Heat Pipe Heat Exchanger for Nuclear Electric Propulsion Power Conversion System

Dennis Nikitaev[1], Corey D. Smith[1], Matthew Duchek[2], Christopher Harnack[2], and William Machemer[2]

[1]*Advanced Projects Huntsville, Analytical Mechanics Associates, Huntsville, AL, 35806*
[2]*Advanced Projects Denver, Analytical Mechanics Associates, Denver, CO, 80211*

Heat pipe reactors have been considered by the Space Nuclear Propulsion program for Nuclear Electric Propulsion (NEP) power conversion systems and will require the use of heat exchangers to transfer heat transported via heat pipes from the reactor to the Brayton working fluid. This analytical work considers Sodium (Na) and lithium (Li) working fluids inside heat pipes which serve as tubes arranged in a rectangular duct to form the heat exchanger. Based on this geometry, Zukauskas correlations are used to model the convective heat transfer and pressure losses. Parametric sizing of the reactor component involved operational limits-based heat pipe modeling in cohesion with required user input geometry for the in-core lattice and various subcomponents.

This work considered various power conversion inlet temperatures (PCIT) of 1100 K, 1150 K, and 1200 K for Na heat pipes and 1100 K, 1150 K, 1200 K, and 1400 K for Li heat pipes for each PCIT, the masses and pressure losses of the combined heat exchanger and reactor subsystem were determined and analyzed. Na showed a lower overall operating temperature and about a fifth of the maximum heat throughput capability than that of Li for the same geometry. Due to this, the entire Na-based subsystem ended up being three times more massive than the Li-based subsystem given five times the required number of heat pipes. At the low PCIT of 1100 K, the Na-based subsystem exhibited the lowest pressure losses given the large overall cross sectional flow area and relatively low frictional pressure losses. However, as the PCIT increased, the frictional pressure losses increased resulting in higher pressure losses at the 1200 K PCIT than Li-based subsystem. The Li-based subsystem exhibited the largest pressure losses of all analyzed cases at the 1400 K PCIT due to the low density of the Brayton working fluid at this temperature.

Nomenclature

Symbols

A_c	=	Cross-sectional Area, m^2
A_s	=	Surface Area, m^2
c	=	Specific heat capacity, J/kg-K
c_p	=	Specific heat capacity at constant pressure, J/kg-K
d	=	Diameter, m
g	=	Gravitational acceleration, m/s^2

[1] Aerospace Systems Engineer, Advanced Projects, AIAA Member
[2] Aerospace Engineering Manager, Advanced Projects, AIAA Member
[3] Aerospace Engineer, Advanced Projects
[4] Aerospace Engineer, Advanced Projects
[5] Insert Job Title, Department Name, and AIAA Member Grade (if any) for fourth author (etc.).

h_{fg}	=	Latent heat of fusion, J/kg
k	=	Thermal conductivity, W/m-K
L	=	Length, m
N	=	Mesh number
P	=	Pressure, Pa
Pr	=	Prandtl number
$\dot{Q}$	=	Heat transfer rate, W
R	=	Ideal gas constant, J/kg-K
Re	=	Reynolds Number
S, P	=	Pitch, m
T	=	Temperature, K
V	=	Velocity, m/s
ρ	=	Density, kg/m^3
σ	=	Surface tension, N/m

Subscripts

adia	=	Adiabatic region
avg	=	Average
cond	=	Condenser region
D	=	Diagonal (Pitch)
eff	=	Effective
eq	=	Equivalent
evap	=	Evaporator region
HP-in	=	Inner part of the shell of the heat pipe
L	=	Longitudinal (Pitch)
liq	=	Liquid
o	=	Outer
T	=	Transverse (Pitch)
thru	=	Throughput

tot	=	Total
vap	=	Vapor
w	=	Wire
wick	=	Wicking region

I. INTRODUCTION/BACKGROUND

Currently, NASA is considering Nuclear Electric Propulsion (NEP) as potential propulsion technologies for a crewed mission to Mars. Electric propulsion systems that have been flight tested relied on solar energy. Solar Electric Propulsion (SEP) has been used in small spacecraft and space exploration probes such as the BepiColombo mission to Mercury [1]. The Systems for Nuclear Auxiliary Power 10A (SNAP-10A) was the world's first nuclear reactor in space as well as the first NEP system since the reactor powered an ion thruster system in orbit resulting in NEP being flight tested. Current electric propulsion technologies that have been ground tested and considered for crewed Mars have very high specific impulse (I_{sp}) in excess of 2000 seconds [1]. Recent work at Analytical Mechanics Associates (AMA) has focused on estimating the mass and performance of NEP systems [4–6].

One of the key elements of NEP is the power conversion system (PCS) shown in Figure 1 which includes the Brayton cycle turbomachinery with the reactor as the heat source, the radiator as the heat sink, and the heat exchangers as the interfaces between the Brayton working fluid and reactor or radiator fluid. The content of this paper will primarily focus on the modeling of heat exchangers which use heat pipes to transfer heat from the reactor heat source to PCS Brayton working fluid. Although analytical and numerical heat pipe studies and analyses have been conducted prior to the present work [8–11], they did not include analyses for NEP heat exchangers which is where the novelty of this work lies.

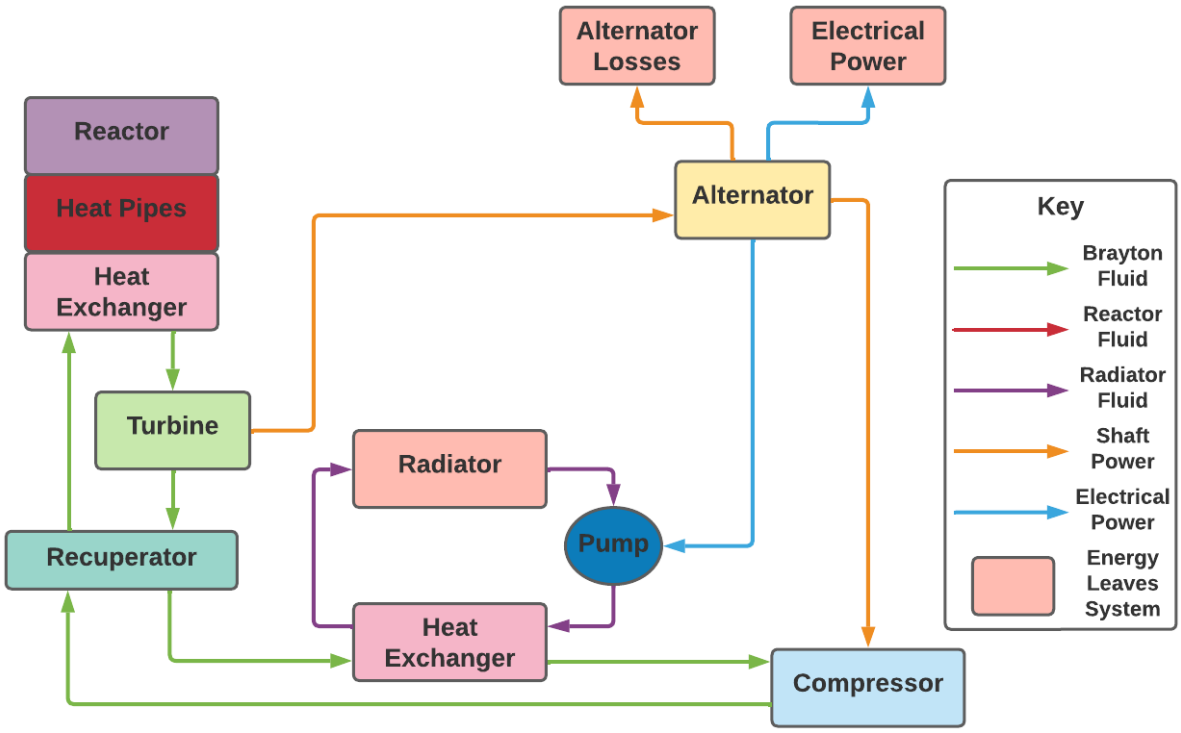

Figure 1: Heat Pipe Brayton Power Conversion System

This work will first walk through a high-level heat pipe limits-based modeling approach which provide a maximum power throughput curve with respect to the operating heat pipe temperature. This curve will be used inside both reactor and heat exchanger models as an isothermal heat source link that transports heat from the reactor to the Brayton fluid. Afterwards, analysis on the subsystem mass and pressure losses will be performed when the Power Conversion Inlet Temperature (PCIT) and the heat pipe working fluid are changed. Due to the large uncertainties in the correlations used, a recommendation of technology down-selection will not be made in this paper.

II. HEAT PIPE MODELING

A. Prior Modeling Efforts

A heat pipe is composed of three key regions: the solid shell, the liquid inside a wick, and the vapor. The working principle of heat pipes is evaporation and condensation of a fluid inside the heat pipe. As shown in Figure 2, the heat pipe is heated on one end where the liquid inside the wick evaporates and this vapor travels through the adiabatic region to the condenser region where the heat is released to the environment when the vapor condenses back to a liquid. The small pressure gradients that are caused by friction flow are responsible for the fluid transfer.

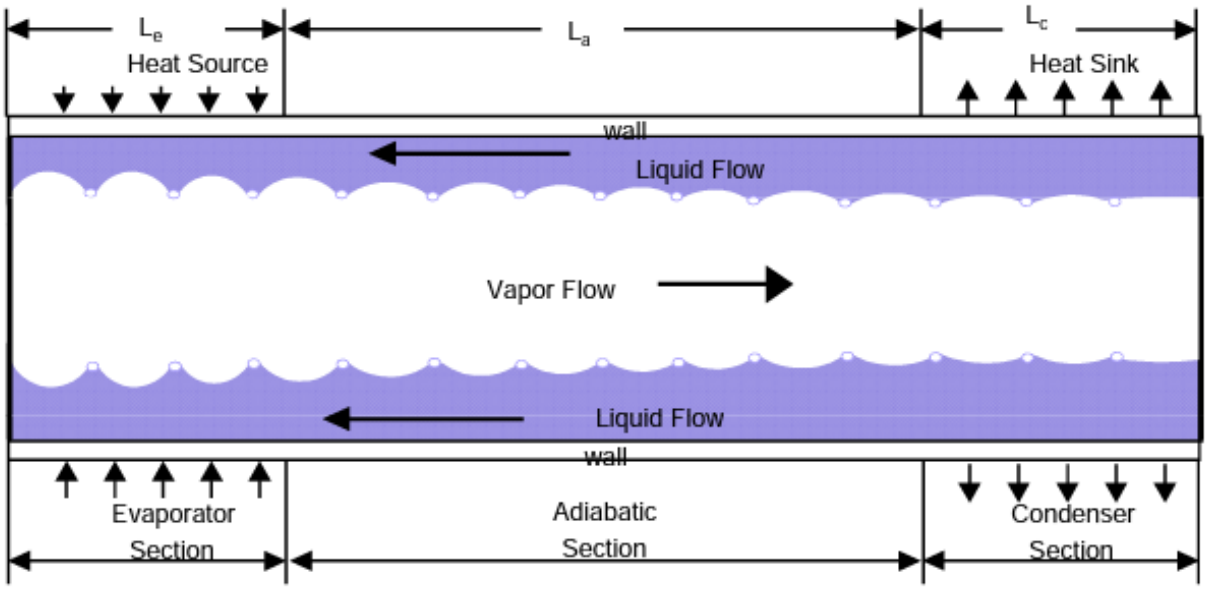

Figure 2: General Heat Pipe Operation [14]

The flow of the vapor results in a high effective thermal conductivity if the heat pipe was to be modeled as a solid rod which was the premise of Zuo & Faghri's model [15]. Due to this simplification, a resistance network model is possible with the schematic shown in Figure 3. Here, the evaporator heat input $\dot{Q}_e$ flows through radial resistances indicated by resistors 1, 2, 3, & 4 in parallel to the axial resistors 5 & 6. Zuo & Faghri's model [15] assumed that the same heat coming into the evaporator was going through the entire heat pipe and rejected to the environment by convective heat transfer indicated by resistor 7.

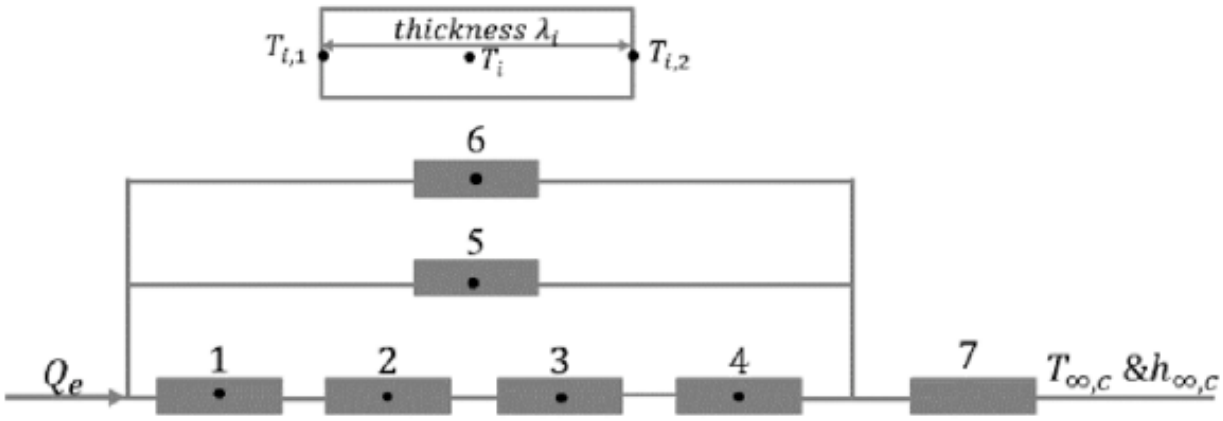

Component	Description
Q_e	Evaporator heat input
1	Evaporator wall (radial direction)
2	Evaporator wick (radial direction)
3	Condenser wick (radial direction)
4	Condenser wall (radial direction)
5	Adiabatic wick (axial direction)
6	Adiabatic wall (axial direction)
7	Convective cooling condition (condenser outer surface)

Figure 3: Resistance Network Schematic for Heat Pipe Operation [16]

Guo et al. [16] took this a step further and included n number of resistors within each resistor number and also implemented transient operation by solving the heat equation shown in Eq. 1 within each resistor. However, this model assumed that the radial heat transfer was higher than the axial heat transfer within the evaporator and condenser regions to effectively model the entire heat pipe in one dimension by switching heat transfer modeling from the radial direction at the evaporator section to axial direction at the adiabatic section and back to radial direction at the condenser section. By using this methodology, the Guo et al. [16] model effectively predicted trends in the temperature distribution of the heat pipe but underpredicted both the temperatures and the length of time for the heat pipe to achieve steady state.

$$\rho c_p \frac{\partial T}{\partial t} = \nabla(\nabla kT) + \dot{Q}'''_{gen} \qquad \text{Eq. 1}$$

B. Equivalent Fluid Properties

The heat pipe is composed of three regions as mentioned previously: the solid shell, the liquid inside a wick, and the vapor. The properties of the solid shell are just those of the material itself. To obtain the equivalent properties of the wick, the properties of the wick as well as the fluid inside must be considered. The assumption in this region is that the fluid flow is slow resulting in a negligent impact on the equivalent properties. Furthermore, the liquid along with the wick are also assumed to be homogenous. Using these assumptions, the first step in finding these properties is to consider the void fraction ε based on the mesh number of the wick N and the wire diameter

d_w as shown in Eq. 2. Using this void fraction, the equivalent density $\rho_{wick_{eq}}$ (Eq. 3), specific heat capacity $c_{wick_{eq}}$ (Eq. 4), and thermal conductivity $k_{wick_{eq}}$ (Eq. 5) of the wick can be found [17].

$$\varepsilon = 1 - 0.2625\pi N d_w \quad \text{Eq. 2}$$

$$\rho_{wick_{eq}} = \varepsilon\rho_{liq} + (1-\varepsilon)\rho_{wick} \quad \text{Eq. 3}$$

$$c_{wick_{eq}} = \varepsilon c_{liq} + (1-\varepsilon)c_{wick} \quad \text{Eq. 4}$$

$$k_{wick_{eq}} = k_{liq}\frac{\left(k_{liq}+k_{wick}\right) - (1-\varepsilon)\left(k_{liq}-k_{wick}\right)}{\left(k_{liq}+k_{wick}\right) + (1-\varepsilon)\left(k_{liq}-k_{wick}\right)} \quad \text{Eq. 5}$$

The fluid properties of the vapor are those of the fluid in the vapor state flowing through the vapor space. However, since the velocity of the flow is significantly higher than that of the liquid inside the wick, an equivalent thermal conductivity of the vapor space must be determined while both ρ and c_p remain the same. First, the pressure drops inside the evaporator ΔP_{evap}, adiabatic ΔP_{adia}, and condenser ΔP_{cond} sections must be calculated and summed to determine the total vapor pressure losses ΔP_{vap} as per Eq. 6.

$$\Delta P_{vap} = \Delta P_{evap} + \Delta P_{adia} + \Delta P_{cond} \quad \text{Eq. 6}$$

Eq. 7 shows the expression for ΔP_{evap}. The friction factor f (Eq. 8) is determined based on the Reynolds number Re_D (Eq. 9) which is calculated based on the diameter of the vapor space d_{vap}. Re_r (Eq. 10) is the radial Reynolds number which helps Eq. 7 account for the radial pressure losses. [8,18,19]

$$\Delta P_{evap} = \left(\frac{Q_{thru}}{h_{fg}}\right)^2 \frac{16 L_{evap} f}{\pi^2 \rho_{vap} d_{vap}^5}(1 + 0.61 Re_r) \quad \text{Eq. 7}$$

$$f = \begin{cases} \dfrac{16}{Re_D} & Re_D < 2000 \\ 0.079 Re_D^{-0.25} & 2000 < Re_D < 20000 \\ 0.046 Re_D^{-0.20} & 20000 < Re_D \end{cases} \quad \text{Eq. 8}$$

$$Re_D = \frac{4\dot{Q}_{thru}}{\pi d_{vap} h_{fg} \mu_{vap}} \quad \text{Eq. 9}$$

$$Re_r = -\frac{4\dot{Q}_{thru}}{2\pi L_{evap} h_{fg} \mu_{vap}} \quad \text{Eq. 10}$$

Eq. 11 shows the expression for ΔP_{adia}. [8,18,19]

$$\Delta P_{adia} = \frac{32\mu_{vap}V_{vap}L_{adia}}{d_{vap}^2}\left[1 + \frac{1 + 0.106Re_r}{18 + 5Re_r} \times \frac{1 - \exp\left(-\frac{60L_{adia}}{Re_D d_{vap}}\right)}{\frac{2L_{adia}}{Re_D d_{vap}}}\right] \quad \text{Eq. 11}$$

Eq. 12 shows the expression for ΔP_{cond} where α is the velocity profile shown in Eq. 13. Here, it is shown that Re_r can be negative which stems from Eq. 10 and the use of the heat transfer as a variable in its definition. [8,18,19]

$$\Delta P_{cond} = \begin{cases} -\frac{16\mu_{vap}V_{vap}L_{cond}}{d_{vap}^2}\left[1 - Re_r\left(\frac{7}{9} - \frac{8\alpha}{27} + \frac{23\alpha^2}{405}\right)\right] & Re_r > -2.25 \\ \frac{-(Re_r + 2)}{\rho_{vap}\left(-1.23Re_r + \frac{2L_{evap}}{L_{cond}}\right)}\left(Re_D\frac{\mu_{vap}}{d_{vap}}\right)^2 & Re_r < -2.25 \end{cases} \quad \text{Eq. 12}$$

$$\alpha = \frac{15}{22}\left[5 + \frac{18}{Re_r} + \sqrt{\left(5 + \frac{18}{Re_r}\right)^2 - \frac{44}{5}}\right] \quad \text{Eq. 13}$$

To determine the equivalent thermal conductivity, the Clausius-Clapeyron equation (Eq. 14) [20] is chosen to describe the relationship between temperature and pressure [16]. Since both the temperature difference and pressure drops are assumed to be small, the properties are assumed to be constant. The temperature difference within the vapor space ΔT_{vap} can then be described by the pressure losses as shown in Eq. 15 [16].

$$\frac{dP}{dT} = \frac{\rho_{vap}h_{fg}}{T} \quad \text{Eq. 14}$$

$$\Delta T_{vap} = \left(\frac{T}{\rho_{vap}h_{fg}}\right)_{avg}\Delta P_{vap} \quad \text{Eq. 15}$$

The axial heat transfer that occurs through the vapor is dependent on the effective length L_{eff} of the heat pipe as shown in Eq. 16 [21].

$$L_{eff} = \frac{L_{evap} + L_{cond}}{2} + L_{adia} \quad \text{Eq. 16}$$

By combining the Clausius-Clapeyron equation with Fourier's Law, the equivalent thermal conductivity of the vapor space is obtained as shown in Eq. 17.

$$\dot{Q}_{thru} = -A_{c_{vap}}k_{vap_{eq}}\nabla T \approx -A_{c_{vap}}k_{vap_{eq}}\frac{\Delta T_{vap}}{L_{eff}} \rightarrow k_{vap_{eq}} = -\frac{\dot{Q}_{thru}L_{eff}}{A_{c_{vap}}\Delta T_{vap}} \quad \text{Eq. 17}$$

C. Heat Pipe Limits

There are five fundamental limits that affect the maximum heat throughput possible through the heat pipe which include viscous, sonic, entrainment, capillary, and boiling limits which are shown in Eq. 18 through Eq. 22, respectively. Even though it is possible for the equivalent thermal conductivity analysis described in the previous section to yield heat transfer rates higher than indicated by these limits, physical phenomena such as the capillary pressure and entrainment of liquid particles into the vapor flow will impact the overall heat transfer performance of the heat pipe. These limits are summarized in Figure 4 with the operation domain shown by the area below the resulting red curve. When starting a heat pipe from a frozen state or operating at cryogenic conditions, the viscous limit is the first limit to be encountered. The next limit that is encountered is the sonic limit which is when the velocity of the vapor exceeds the local speed of sound. Then the entrainment limit occurs when the vapor flowing through the center of the heat pipe begins interfering with the liquid flowing on the sides of the heat pipe which causes the liquid to dry in the evaporator. Then the wicking/capillary/circulation limit provides the most heat transfer and is often the steady state operation mode of the heat pipe. Here, the pressure losses of the vapor and liquid must be balanced or else dry out will occur and the pipe will be damaged. The wick provides capillary pressure and when the ΔP between the wick and the vapor exceeds this pressure, the capillary limit is reached. The Churchill friction factor is used in this limit which has good agreement with experimental data across laminar, transitional, and turbulent flow regimes and is shown in Eq. 23 through Eq. 25 [22]. Lastly, the boiling limit when a significant buildup of vapor bubbles form on the edges of the heat pipe, thus increasing the resistivity of the wick to heat transfer and lead to dry out. [23–26]

$$\dot{Q}_{V_{max}} = \frac{d_{vap}^2 h_{fg} \rho_{vap} P_{vap} A_{c_{vap}}}{64 \mu_{vap} L_{eff}} \quad \text{Eq. 18}$$

$$\dot{Q}_{S_{max}} = A_{c_{vap}} \rho_{vap} h_{fg} \sqrt{\frac{\gamma R T_{vap}}{2(\gamma + 1)}} \quad \text{Eq. 19}$$

$$\dot{Q}_{E_{max}} = A_{c_{vap}} h_{fg} \sqrt{\frac{\rho_{vap} \sigma}{d_{cond}}} \quad \text{Eq. 20}$$

$$\dot{Q}_{C_{max}} = \frac{\frac{2\sigma}{r_c} - \rho_{liq} g \left(d_{vap} \cos\theta + L_{tot} \sin\theta \right)}{\left(f_{liq} + f_{vap} \right) L_{eff}} \quad \text{Eq. 21}$$

$$\dot{Q}_{B_{max}} = \frac{\frac{4\pi L_{evap} k_{wick_{eq}} T_{vap} \sigma}{r_n h_{fg} \rho_{vap} \ln \frac{d_{HP-in}}{d_{vap}}}}{1 + \frac{2\pi L_{evap} k_{wick_{eq}} T_{vap} L_{eff} \mu_{liq}}{K h_{fg} A_{c_{wick}} \rho_{liq} h_{fg} \rho_{vap} \ln \frac{d_{HP-in}}{d_{vap}}}} \quad \text{Eq. 22}$$

$$f_{CH} = 8\left[\left(\frac{8}{Re}\right)^{12} + \frac{1}{(A+B)^{1.5}}\right]^{1/12} \quad \text{Eq. 23}$$

$$A = \left[2.457 \ln\left(\frac{1}{\left(\frac{7}{Re}\right)^{0.9} + 0.27\frac{\varepsilon}{d}}\right)\right]^{16} \quad \text{Eq. 24}$$

$$B = \left(\frac{37530}{Re}\right)^{16} \quad \text{Eq. 25}$$

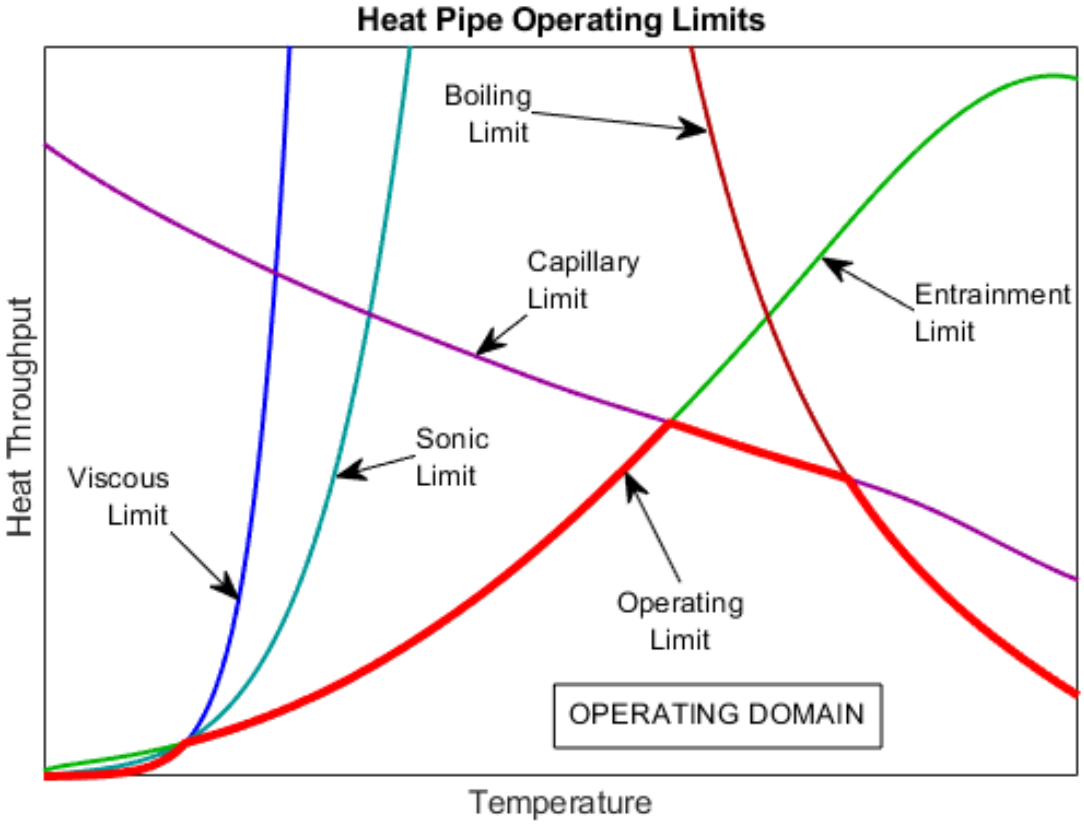

Figure 4: Heat Pipe Limits Summary

This model is validated against numerical and experimental results from bench top experiments using sodium heat pipes at various operating temperatures which were based on the Kilopower Reactor Using Sterling Technology (KRUSTY) unit [16]. Their physical parameters are found in Table 3. In the benchtop experiment, the heat pipe was not a thermosyphon as was used in KRUSTY as no assistance from gravity was incorporated given that the heat pipe was horizontal during testing. The validation results are shown in Figure 5 where close agreement is observed between both the numerical model and experiment. Based on thermofluid model-model validation (acceptable within 4%) and model-experiment validation (acceptable within 8%) guidelines [27], this relative error (<3%) is acceptable. Therefore, based on this, the heat pipe limits model is validated.

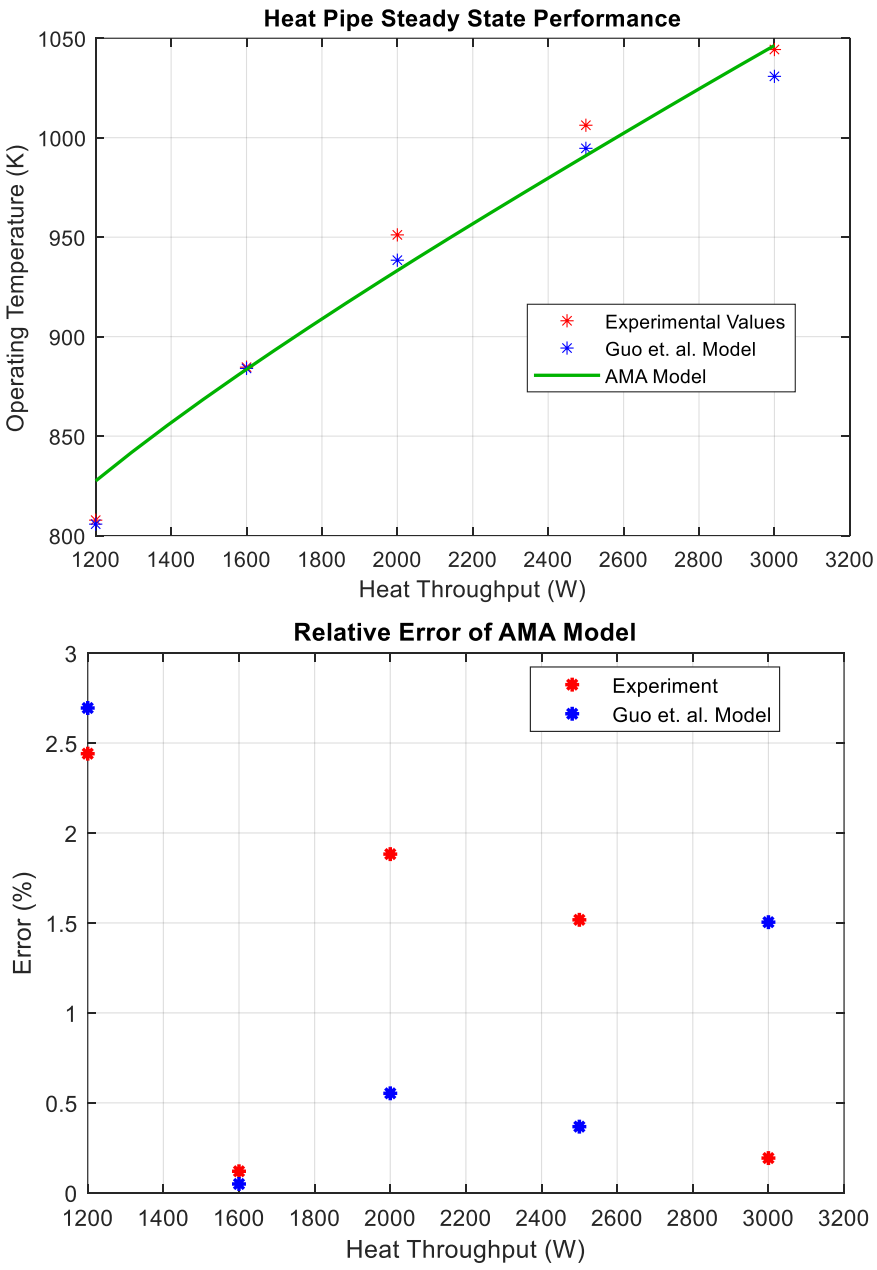

Figure 5: Heat Pipe Limits Validation [16]

Table 3: Validation Heat Pipe Parameters [16]

Description	Value	Units
Length of Evaporator	300	mm
Length of Adiabatic Section	300	mm
Length of Condenser	400	mm
Outer Diameter	20	mm
Inner Diameter of Vapor Space	14	mm
Wall Thickness	2	mm
Wick Thickness	1	mm
Mesh Number	300	-
Wall Material	316 L Stainless Steel	-
Wick Material	316 L Stainless Steel	-

III. REACTOR MODELING

To approach NEP system performance modeling, a comprehensive reactor module is crucial to calculate key operating conditions and case-specific component masses. Based on past literature, reactor design options include direct drive gas-cooled, pumped liquid metal, and passive heat pipe concepts. Heat pipe and pumped liquid metal reactors will require a heat exchanger to interface with the PCS. The focus of this work will be set on the heat pipe reactor and its heat exchanger.

Convergence on required reactor dimensions is heavily dependent on the case-specific operating conditions of the Brayton cycle. As shown in Figure 6, the user can specify the reactor unit cell geometry, heat pipe fluid, and the heat exchanger boundary conditions to calculate the final reactor dimensions. In addition, Table 4 provides a summarization of the required inputs and model outputs that are used to inform the heat exchanger sizing calculations. Working fluid inlet temperature/pressure, desired exit temperature, and mass flow rate are used to calculate the enthalpy rise across the heat exchanger and the required reactor thermal power for an input case. The outputs of this model include Reactor Thermal Power, Reactor Mass, External Shield Mass, Number of Fuel/Moderator Heat Pipes, and the Number of Reactor Unit Cells. An important aspect is that the number of reactor cells will scale via integer values subject to the overall reactor geometry resulting in a non-smooth mass approximation for both reactor and shield. This will in turn cause non-smooth mass approximation for the heat exchanger. Details of this model are beyond the scope of this paper; they are planned for a separate publication.

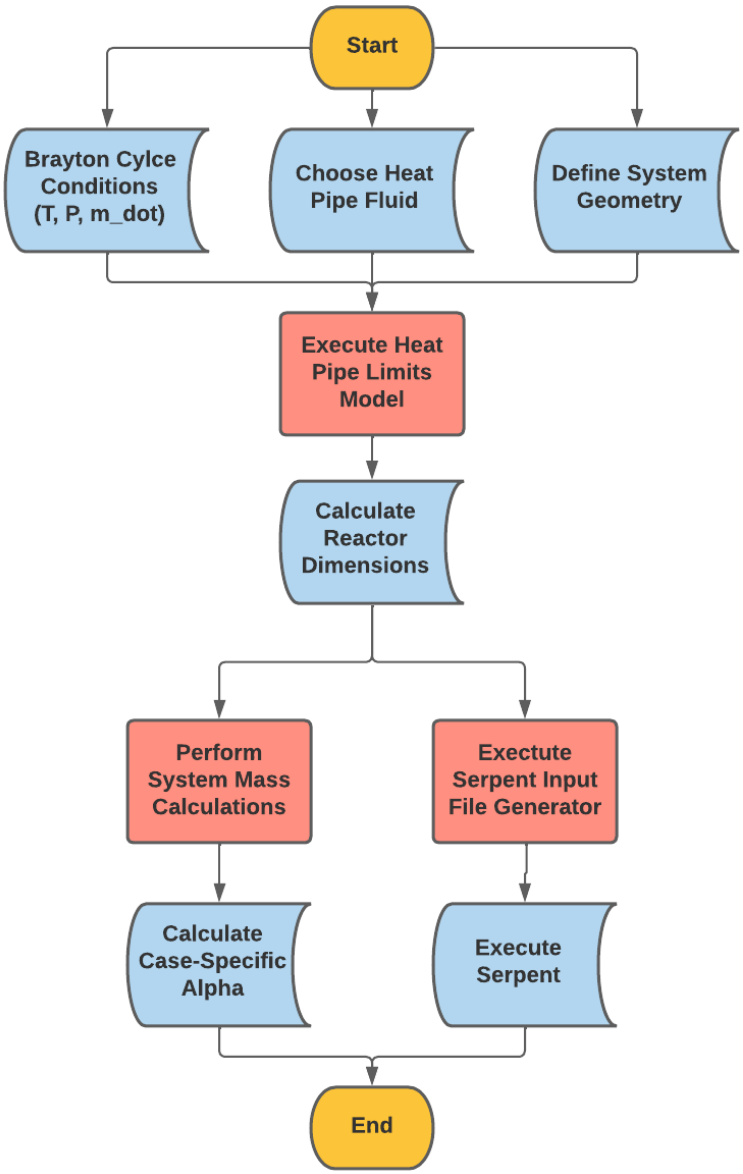

Figure 6: Heat Pipe Reactor Sizing Algorithm

Table 4: Heat Pipe Reactor/Heat Exchanger Inputs and Ranges

Inputs	Input Parameter Range	Units
HX Mass Flow Rate	5 to 100	kg/s
HX Inlet Gas Temperature	700 to (PCIT - 100)	K
Power Conversion Inlet Temperature (PCIT)	1100 - 1400	K
HX Inlet Gas Pressure	1 to 4.5	MPa
Heat Pipe Film Temperature Difference (Wall Temperature - PCIT)	0 to (PCIT-Max HP T)	K
Heat Pipe Throughput Factor	50 to 90	%

To generate the heat pipe reactor trade space, parametric analyses are performed by varying the six inputs in the range of expected conditions. Outputs of the convergence model are stored into large, multidimensional arrays for spline interpolation. Use of spline curves allow the performance models to predict reactor performance with high confidence for any intermediate heat exchanger boundary condition. The number of heat pipes in the reactor (fuel and moderator) and their dimensions serve as inputs to the heat exchanger sizing model. While the heat pipe pitch is defined in the reactor geometry, the heat exchanger solver can vary the pitch since bending heat pipes is a viable option [9,28].

As discussed previously, the reactor modeling suite is focused on parametric sizing and optimization based on point-design unit cells. To assess the mass of the reactor, room-temperature material densities are used to analyze the launch mass of the reactor components. In addition, the sizing algorithm determines the number of unit cells to reach thermal hydraulic convergence. The total mass of the reactor active core is calculated by scaling the per unit cell mass with the converged quantity. The masses of the reflector and pressure vessel (if required) are calculated after the active core dimensions are determined. Additional subcomponent masses, such as structural support and instrumentation/control, are calculated using scaling correlations from the SP-100 project [29].

In the current modeling suite, the external radiation shield consists of tungsten (W) for gamma shielding and lithium hydride (LiH) for neutron shielding. The reactor sizing algorithm will determine the core radius which will vary the required shielding radii. Thicknesses are set by the user and are informed by heritage space reactor designs [30]. Future iterations of the tool will perform parametric sizing of the external shield thicknesses based on radiation attenuation and dose requirements for the radiator and power conversion system.

IV. HEAT EXCHANGER MODELING

A. Model Description

To simplify the analysis, the heat exchanger type will be assumed to be a tube bank heat exchanger which is one of the recommended heat exchanger designs from past work for high temperature heat exchanger applications [11]. The tubes in this design represent the heat pipes. The model calculates the required heat exchanger and accompanying reactor with shield based on the inputs provided. These inputs include the inlet conditions (temperature, pressure, and mass flow rate) of the Brayton fluid, heat pipe definition characteristics that supply the information required by Eq. 18 through Eq. 25, heat pipe layout within the heat exchanger (inline or staggered), desired outlet temperature, and materials used for the heat pipes and heat exchanger. The outputs provided include the fluid state at outlet from the heat exchanger; masses of the heat exchanger, reactor, and shield; effectiveness; pressure losses; and total heat transferred. Since the reactor is optimized based on the heat transfer required and inlet conditions, the integrated reactor code supplies the information regarding the total number of heat pipes that are to be arranged within the heat exchanger using the specified arrangement scheme. This is done by first assuming a uniform longitudinal and transverse pitch and then adjusting the pitch of the heat pipes by using either Eq. 26 for an inline arrangement or Eq. 27 for a staggered arrangement. These equations were constructed based on the total number of heat pipes using the allocated linear spacing per heat pipe which includes the heat pipe diameter summed with the pitch.

$$N_{HP_{inline}} = N_{HP_W} N_{HP_L} = \frac{L_{HX}}{D_{HP} + S_{HP}} \frac{W_{HX}}{D_{HP} + S_{HP}} \rightarrow S_{HP}^2 + 2D_{HP}S_{HP} + D_{HP}^2 = \frac{L_{HX} W_{HX}}{N_{HP_{inline}}} \quad \text{Eq. 26}$$

$$N_{HP_{stag}} = \frac{N_{HP_L}}{2} N_{HP_W} + \frac{N_{HP_L}}{2}\left(N_{HP_W} - 1\right) = N_{HP_L}\left(N_{HP_W} - \frac{1}{2}\right) = \frac{L_{HX}}{D_{HP} + S_{HP}}\left(\frac{W_{HX}}{D_{HP} + S_{HP}} - \frac{1}{2}\right) \quad \text{Eq. 27}$$

The mass is calculated by determining the required thickness of the heat exchanger walls based on the pressure of the Brayton working fluid and the yield strength of the specified material at the desired outlet temperature based on stress calculations for a plate with a uniform load [31]. It is assumed that the system operates at a perfect vacuum resulting in a ΔP equal to the pressure of the working fluid for a conservative estimation. The heat pipe mass accounts for the outer shell of the heat pipe and includes the mass of the working fluid which assumes that the liquid portion completely occupies the wall to wick region. The total mass of the system is the summation of the heat exchanger, heat pipes, reactor, and shield.

The values that are optimized are the length (L) and width (W) of the heat exchanger, the surface temperature of the heat pipe, and the fraction of the maximum heat throughput of the heat pipe. The latter parameter is required by both reactor and heat exchanger models to fine tune the power transferred and required outlet temperature, respectively since the number of heat pipes is dependent on the reactor and cell geometry. This is a valid parameter of optimization since the heat pipe limits discussed in Section II.C specify only the maximum heat transfer rate at any given temperature with the operating regime being valid anywhere below the heat throughput curve shown in Figure 4 [21,23–26]. The height (H) of the heat exchanger remains constant due to that being equal to the condenser length of the heat pipes. A CAD concept of the heat exchanger portion of the subsystem is shown in Figure 7 where the W, L, and H dimensions are labelled along with the tube representation of the heat pipes.

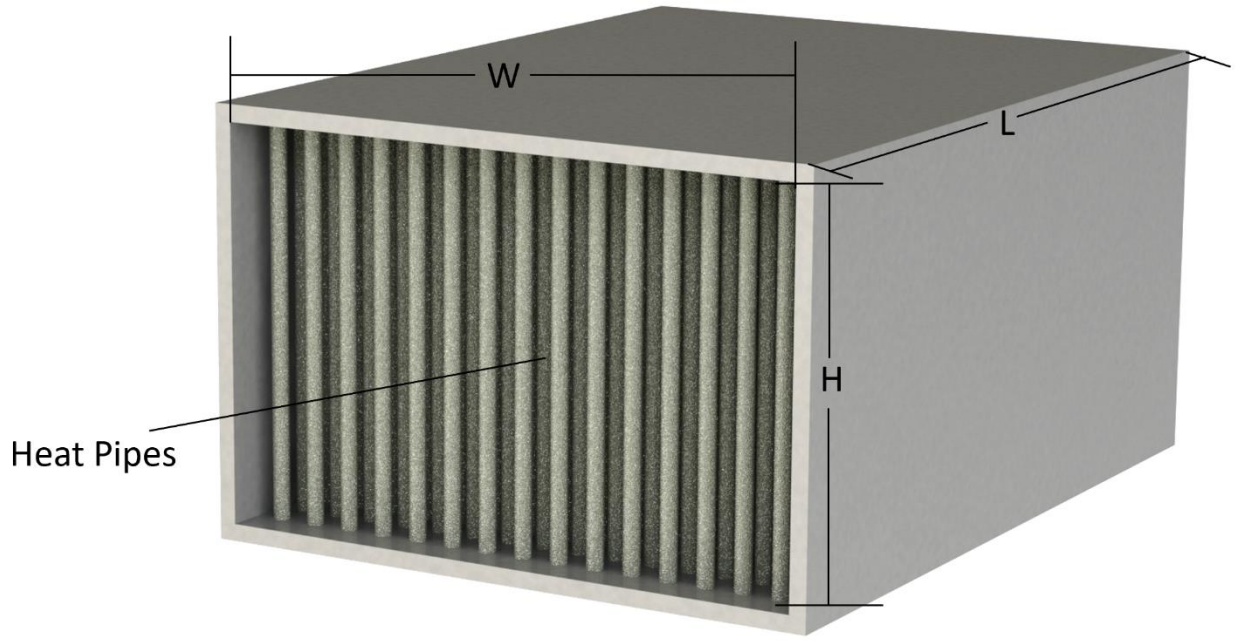

Figure 7: Heat Exchanger Geometry

The optimization routine used considers minimizing the total mass of the components and adhering to the specified outlet temperature. Since these optimizations result in two equations with four unknowns, the Levenberg-Marquardt algorithm is used for the under-constrained system. To implement this algorithm, a modified `fminsearch` called `fminsearchbnd` [32] MATLAB function is used with specified bounds which limit the solution to be within reasonable bounds such as to not violate basic heat transfer physics of a heat pipe temperature below the desired outlet temperature, provide positive and finite values for the heat exchanger dimensions, and not exceed 100% of the heat pipe heat throughput limits. Furthermore, it was found that the least squares solver for a non-linear systems of equations `lsqnonlin` resulted in very long solution times, was not more accurate, and did not fit well with the input parameter sweeps which will be discussed later in this paper. Similarly, a global solution method was not used due to long computational times and a general initial guess approach was used instead. However, since the system of equations is unconstrained, local minima were found instead of the global minima. Better optimization could be achieved by manually modifying the initial guesses specific to a performance regime resulting in up to a 13% decrease in the mass in selected cases. This results in a relatively high uncertainty in the results simply based on the optimization regime used. Furthermore, the physics-based heat transfer model, which will be discussed next, adds more uncertainty based on experimental comparison with the heat transfer model. Overall, this model results in conservative mass estimates of the system that can be used in higher level system modeling.

The methodology for modeling the tube cross flow will be taken from Zukauskas for which the general form of the correlation is shown in Eq. 28 where the constants *a* and *b* change according to the *Re* and tube arrangement [33]. The fluid that will participate in heat transfer in external flow through the tube bank is the $He_{0.72}Xe_{0.28}$ mixture which is consistent with past experimental work on the Brayton Rotating Unit (UNM-BRU-3) [34]. This mixture has an average Pr of around 0.208 according to the properties found on NIST [35] and in the CoolProp thermophysical and transport

property library [36]. Furthermore, although textbooks claim that the Pr range is above 0.7 for the Zukauskas correlations [37–39], other sources have stated that these correlations have low error for Pr above 0.4 and the error for a Pr of 0.2 would be up to 24% [40,41]. However, no correlations exist in literature that are specific to a noble gas mixture flow through a bank of tubes. Further research must be done for noble gas mixture flow through tube banks, and it was proposed to simply modify the exponent of Pr in the Zukauskas correlations to better fit this data [41].

$$Nu = aRe^{b}Pr^{0.36}\left(\frac{Pr}{Pr_s}\right)^{0.25} \quad \text{Eq. 28}$$

Zukauskas also provided graphical representations of the variations of the friction factor f and correction factor χ for the pressure loss correlation shown in Eq. 29 through N_L number of tube rows along the flow path [33]. The data from these curves was extracted via GrabIt [42] and was spline fitted by performing two-dimensional interpolation to determine the values given any set of pitch values (longitudinal pith P_L and transverse pith P_T) and *Re* within the range that these graphs cover (for more information, the reader is advised to refer to the source of these graphs [39]).

$$\Delta P = N_L f \chi \frac{\rho V_{max}^2}{2} \quad \text{Eq. 29}$$

B. Model Results

1. Heat Pipe Heat Throughput Limits

The heat pipe limits have been implemented for a characteristic heat pipe design subjected to the limits discussed in Section II.C. Figure 8 shows the results for Na and Li using the same heat pipe geometry provided by Los Alamos National Laboratory. Important features that are common to both fluids are that the capillary limit is never reached and, instead, the boiling limit imposes the most heat throughput limitation at high temperatures. Furthermore, both the viscous and sonic limits play a role at the lower temperatures which will affect the heat pipe start up regime which future work will analyze. The highest heat throughput rise occurs at the entrainment limit for both fluids.

There are two key differences between the Na and Li operability regimes. The first is that Li will operate at higher temperatures due to its higher boiling point resulting in Na being the more optimal fluid at heat pipe temperatures below 1300 K. The second is that Li will transport over three times more heat than the Na heat pipe of the same geometry, albeit, at a temperature which is over 400 K higher than the maximum heat throughput temperature of Na. All this suggests that the heat pipe steady state operating temperature will guide the heat pipe fluid selection which will further guide the heat throughput per heat pipe. This is an important aspect which must be considered as an iterative design approach will be required to determine the heat exchanger and reactor sizing as the power levels and heat pipe operating temperature regimes are modified.

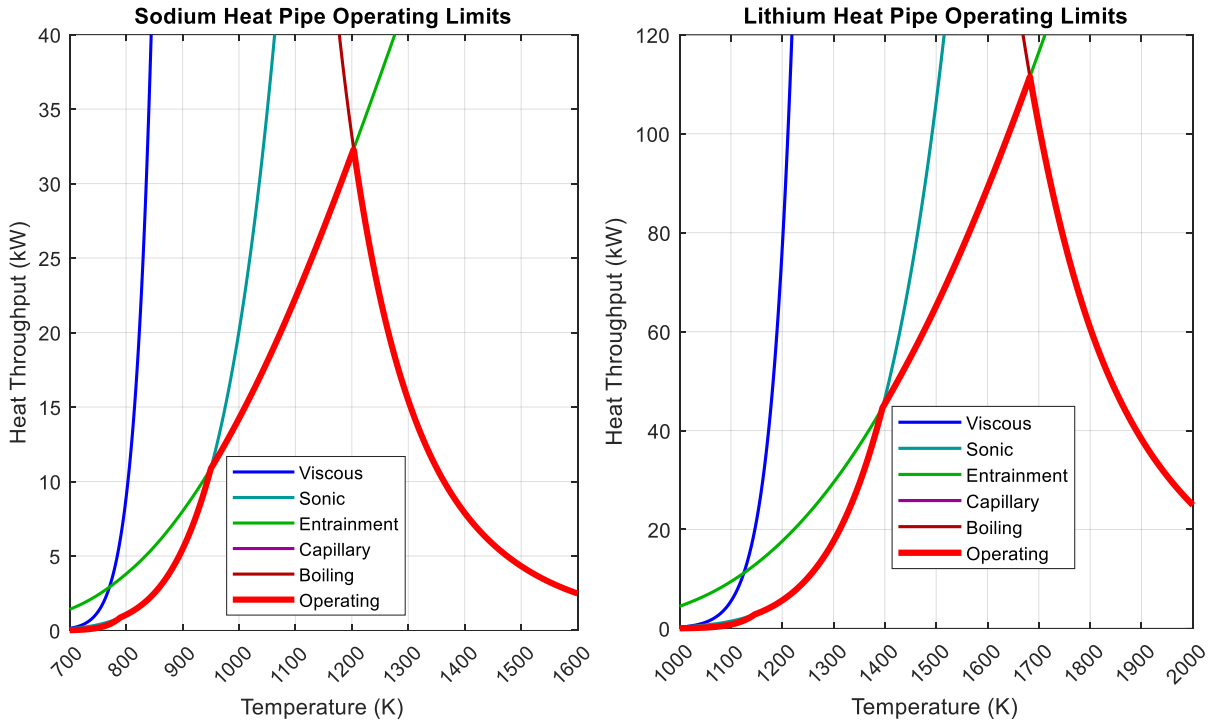

Figure 8: Heat Pipe Heat Throughput Limits: (left) Sodium, (right) Lithium

2. Mass Estimation

Due to the previously discussed solution approach of using a generic initial condition in Section IV.A, the results in this section show the local minima which tend to show a close trend from which fits for the masses of the heat pipe/heat exchanger/reactor/shield subsystem can be obtained with respect to the varying inlet conditions. An example of such a data set is shown in this paper for Li heat pipes with a desired outlet temperature of 1200 K. Table 4 shows the ranges of the inlet conditions that were examined and Figure 9 through Figure 11 show the resulting masses where the parameters not shown on the x-axis are taken to be the direct middle of their respective ranges. As shown, the data tends to form curves against which fits have been made. The approach to the fits stemmed from thermofluids [43] and historical mass relations [44] by taking a single fit and adding dimensionless modifiers as scaling factors. For this system, the mass flow rate fit served as the dimensioned parameter as the system grows the most with this parameter while the temperature and pressure fits were non-dimensionalized by using an arbitrary reference mass taken to be in the middle of each inlet parameter that was swept as shown in Eq. 30. Moreover, powers *a*, *b*, and *c*, were used to modify the individual fits to adhere closely to the data when the fit function is put together.

These results show that the subsystems with the lowest mass result from a low flow rate, high inlet temperature, with a small effect from the inlet pressure which decreases the system mass with decreasing pressure contributed by the heat exchanger. Both inlet pressure and temperature parameters affect the mass linearly while the mass flow rate increases the heat exchanger mass exponentially and the reactor/shield components logarithmically. Despite this, in all cases, the total mass of the entire subsystem has a relatively linear behavior with each respective parameter. The heat exchanger mass is primarily affected by the total heat throughput which translates to lower mass at higher temperature and higher mass at higher flow rates. The secondary mass contribution for this component is the pressure which directly affects the required duct thickness to contain the

working fluid. Similarly, the reactor and shield components are functions of the heat transferred and have negligible impact from the working fluid pressure.

Table 4: Ranges of Inlet Conditions Used in Sweep

Inputs	Input Parameter Range	Units
Mass Flow Rate	5 to 100	kg/s
Inlet Temperature	700 to (PCIT – 100)	K
Outlet Temperature (PCIT)	1100 – 1400	K
Inlet Gas Pressure	0.5 to 4	MPa
Heat Pipe Fluids	Na & Li	-

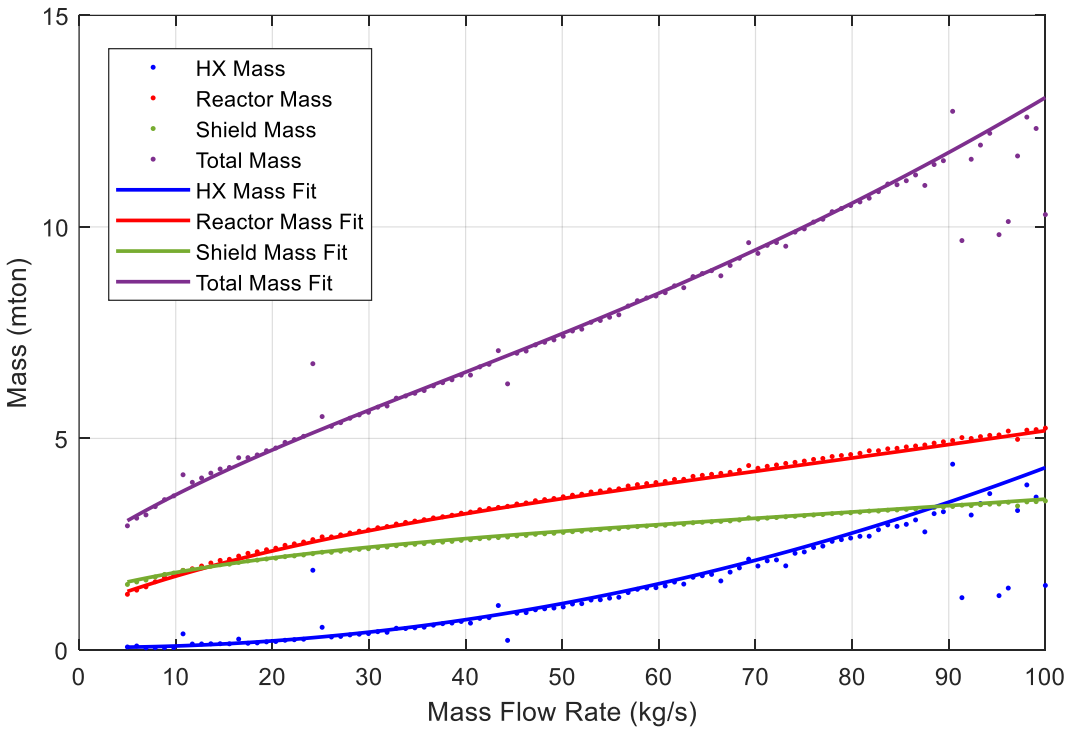

Figure 9: Li, PCIT 1200 K, Mass Flow Rate of Brayton Working Fluid Effect on Mass
Inlet Pressure: 3000 kPa
Inlet Temperature: 850 K

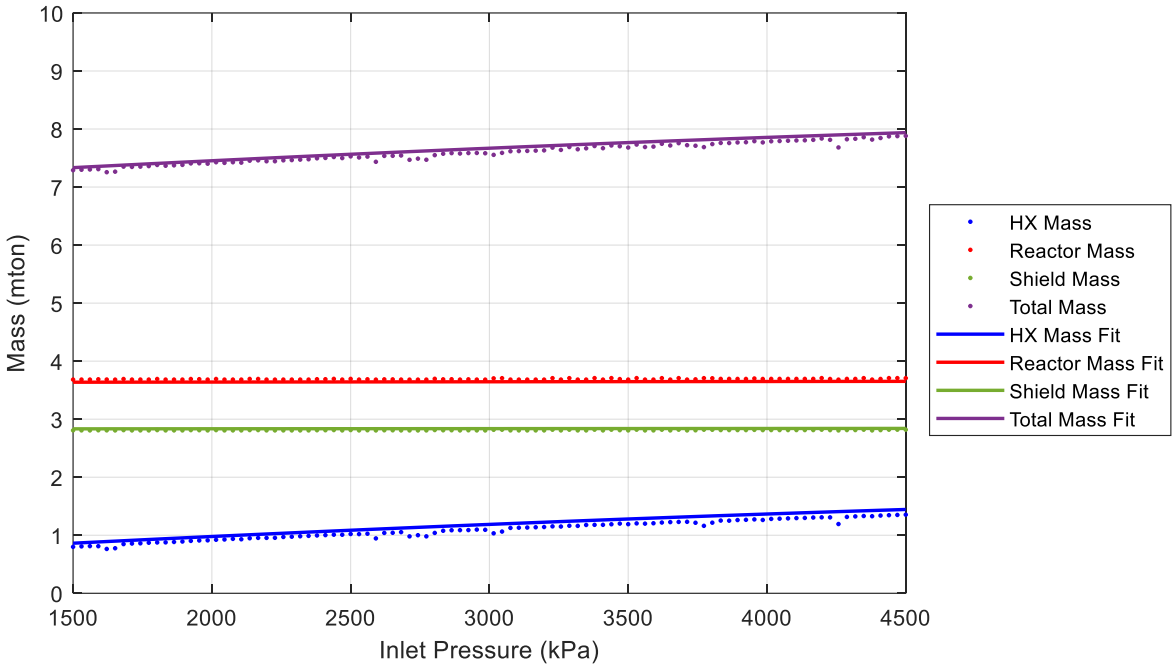

Figure 10: Li, PCIT 1200 K, Inlet Pressure Effect on Mass
Mass Flow Rate of Brayton Working Fluid: 52 kg/s
Inlet Temperature: 850 K

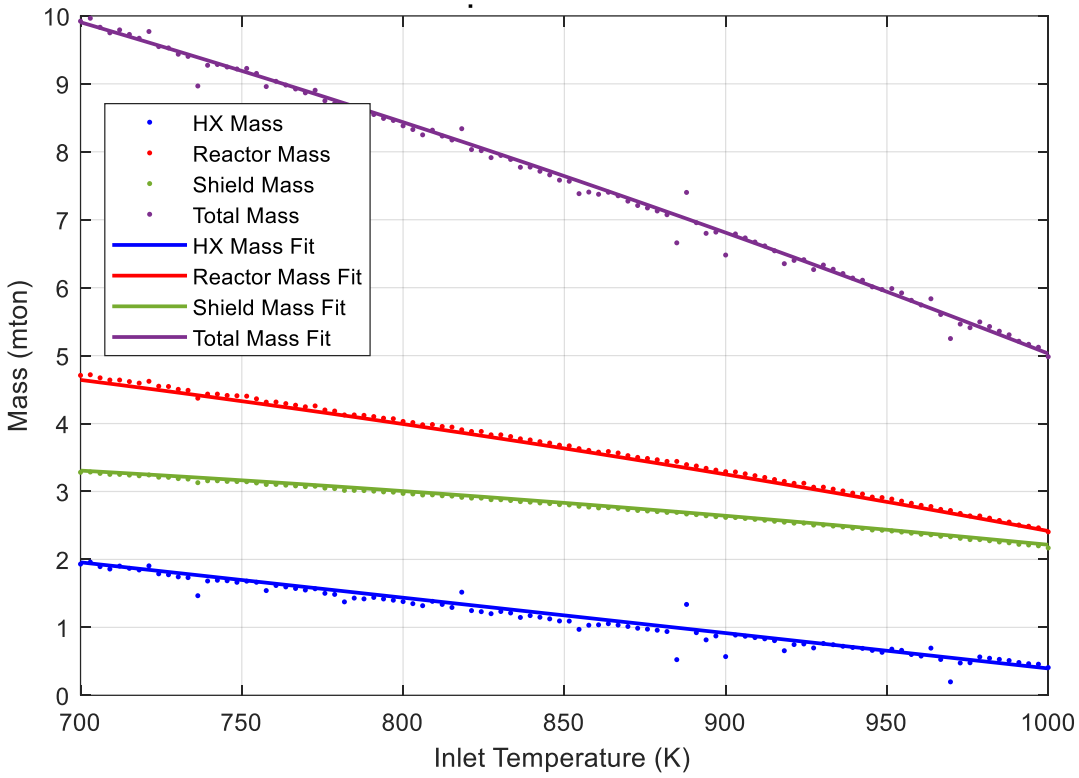

Figure 11: Li, PCIT 1200 K, Inlet Temperature Effect on Mass
Inlet Pressure: 3000 kPa
Mass Flow Rate of Brayton Working Fluid: 52 kg/s

$$m_{fit} = [m_{\dot{m}}(\dot{m})]^a \left[\frac{m_T(T)}{m_{ref}}\right]^b \left[\frac{m_P(P)}{m_{ref}}\right]^c \quad \text{Eq. 30}$$

3. Pressure Loss Effects

The pressure losses are calculated based on the Zukauskas correlations and are not minimized due to their minimization being in direct conflict with the minimization of mass. The mass is minimized, making the heat exchanger smaller and thus making the distances between the heat pipes smaller. However, if pressure losses were to be minimized, then this would lead to a larger overall heat exchanger. Furthermore, the pressure losses at the minimized mass tend to be less than 10 kPa which translates to less than 1% of the inlet pressure – a value that is smaller than assumptions from prior work [45]. General trends are observed in Figure 12 which shows how the resulting ΔP varies as a function of the inlet temperature, inlet pressure, and Brayton working fluid mass flow rate. The trends show that as the inlet temperature increases and the PCIT stays the same, the fluid inside the heat exchanger has a higher average temperature resulting in a lower overall density leading to higher volumetric flow rate and therefore higher pressure losses. As the inlet pressure increases, the density of the working fluid increases leading to lower volumetric flow rate resulting in lower pressure losses. This is results in relatively smooth data since the changes to the subsystem design are minimal. Finally, as the mass flow rate increases, the volumetric flow rate increases resulting in higher pressure losses. The relationship between the pressure losses and inlet temperature and pressure are logarithmic and exponential, respectively while the mass flow rate affects the pressure losses linearly. This is due to the way the volumetric flow rate changes which has a direct effect on the pressure losses which is consistent with expectations provided by Zukauskas and the theory of pressure losses in general [39,46].

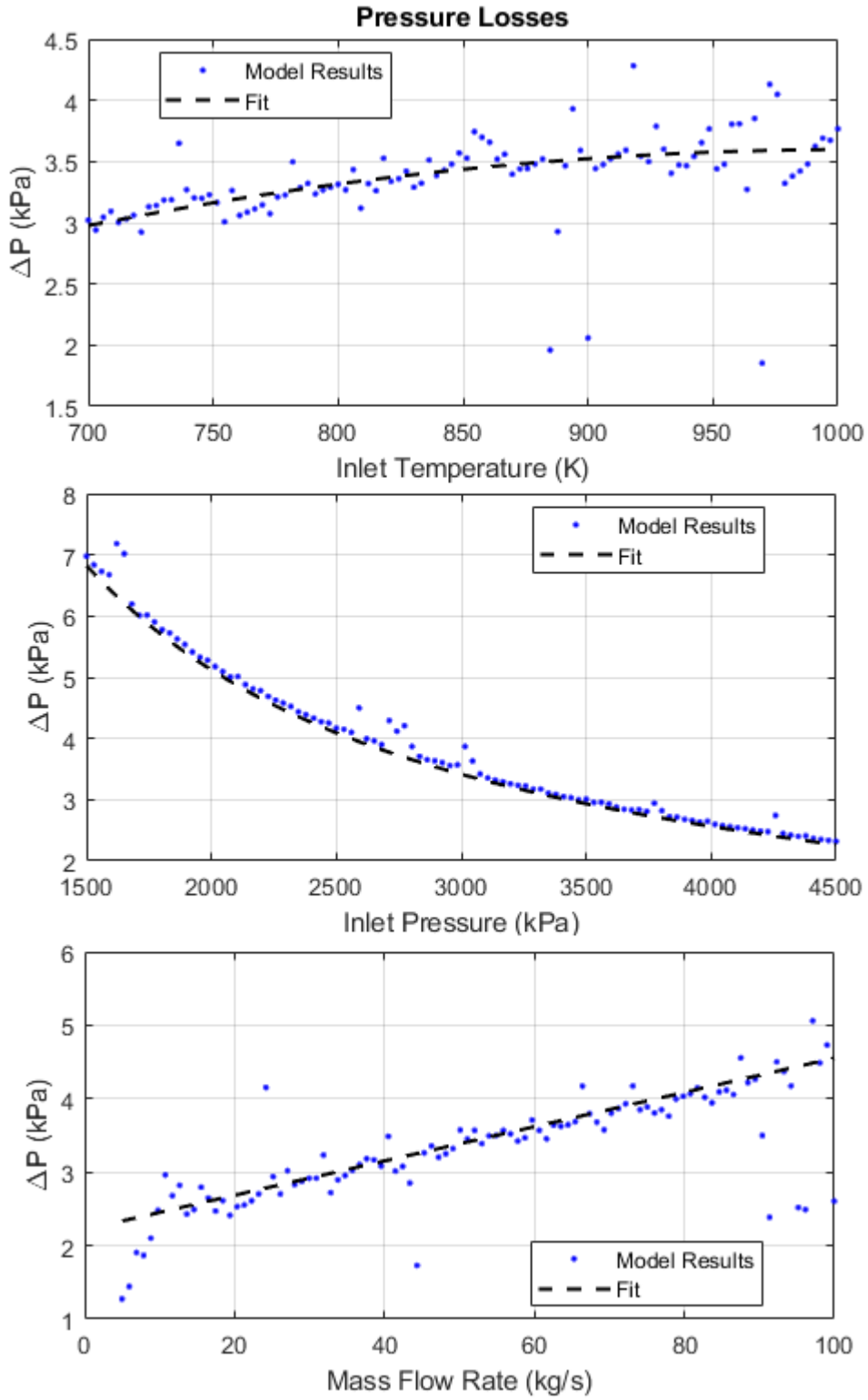

Figure 12: Li, PCIT 1200 K, Inlet Effects on ΔP
(top) Pressure Loss Variation from Inlet Temperature
(middle) Pressure Loss Variation from Inlet Pressure
(bottom) Pressure Loss Variation from Brayton Working Fluid Mass Flow Rate

V. IMPACTS TO THE POWER CONVERSION SYSTEM

A. Definition of Cases for Analysis

The optimal operating points for the PCS were first determined by using a thermodynamic approach which separately modeled the different system components which were shown in Figure 1. Details of the Thermodynamic Model were discussed in detail in previous works [4–6]. The considered PCIT were 1100 K, 1150 K, 1200 K, and 1400 K which are consistent with the operating regimes of the Power Technology Options for NEP [47] and those considered in previous works [4–6]. The optimization criteria was to minimize the specific mass of the system by using the mass curves of Figure 9 through Figure 12 and those for other components built in to the thermodynamic model. This provided the general performance parameters for the PCS which were to be used as inputs, shown in Table 5, to a more detailed component analysis which included the consideration of turbomachinery. Furthermore, the minimum system pressure was determined to be around 1 MPa and the turbine pressure ratio was calculated to be around 2. The details of the Detailed Component Model (DCM) were also discussed in previous work [13]. The described heat pipe model, reactor model, and heat exchanger model and their results were tied into the DCM.

Table 5: Thermodynamic Model Results

Heat Pipe Fluid	PCIT (K)	Max P (MPa)	Min T (K)	$\dot{m}$ (kg/s)	Recup. Eff. (%)
Li	1100.00	2.16	361.000	10.9	94.000
Li	1150.00	2.17	360.969	9.8	93.840
Li	1200.00	2.16	371.912	9.3	93.999
Li	1400.00	2.46	375.708	5.8	93.980
Na	1100.00	2.18	364.752	11.5	93.702
Na	1150.00	2.19	356.800	9.6	93.991
Na	1200.00	2.18	383.816	10.4	93.986

The analysis performed by the DCM required more parameters to solve for the details of the heat pipe/reactor/heat exchanger subsystem to output the required heat pipe temperature, size of heat exchanger, and number of heat pipes alongside the key performance parameters such as the reactor power level and subsystem mass. These additional parameters included the determination of the temperature limits of the respective heat pipe fluids. If the heat pipe operating limits of Na and Li shown in Figure 8 are imposed on top of each other, a comparison of the two fluids immerges as shown in Figure 13. As was discussed in Section IV.B.1, Na should be used for the lower operating temperatures. Furthermore, Figure 13 allows the determination of the temperature ranges to consider when analyzing the power conversion system performance. The temperature limits for the two fluids emerge as 1300 K for Na based on the higher performing Li and 1700 K for Li as temperature above this value exceed the maximum heat throughput.

The operating temperature of the heat pipes should not be confused with the PCIT of the Brayton cycle which will always be lower since the Brayton fluid is heated by the heat pipes. Typically, higher Brayton cycle temperatures result in higher cycle efficiencies and higher temperature differences between the cold and hot fluids or elements inside a heat exchanger result in a smaller component, thus saving mass [6,12]. However, the extent to which this added

performance is technically viable is limited by the materials used [45,47]. Therefore, to adhere to material limitations, a $Mo_{0.7}W_{0.3}$ alloy will be used for both heat pipe shells and heat exchanger duct according to this material's yield strength, thermal conductivity, and density at the considered operating conditions.

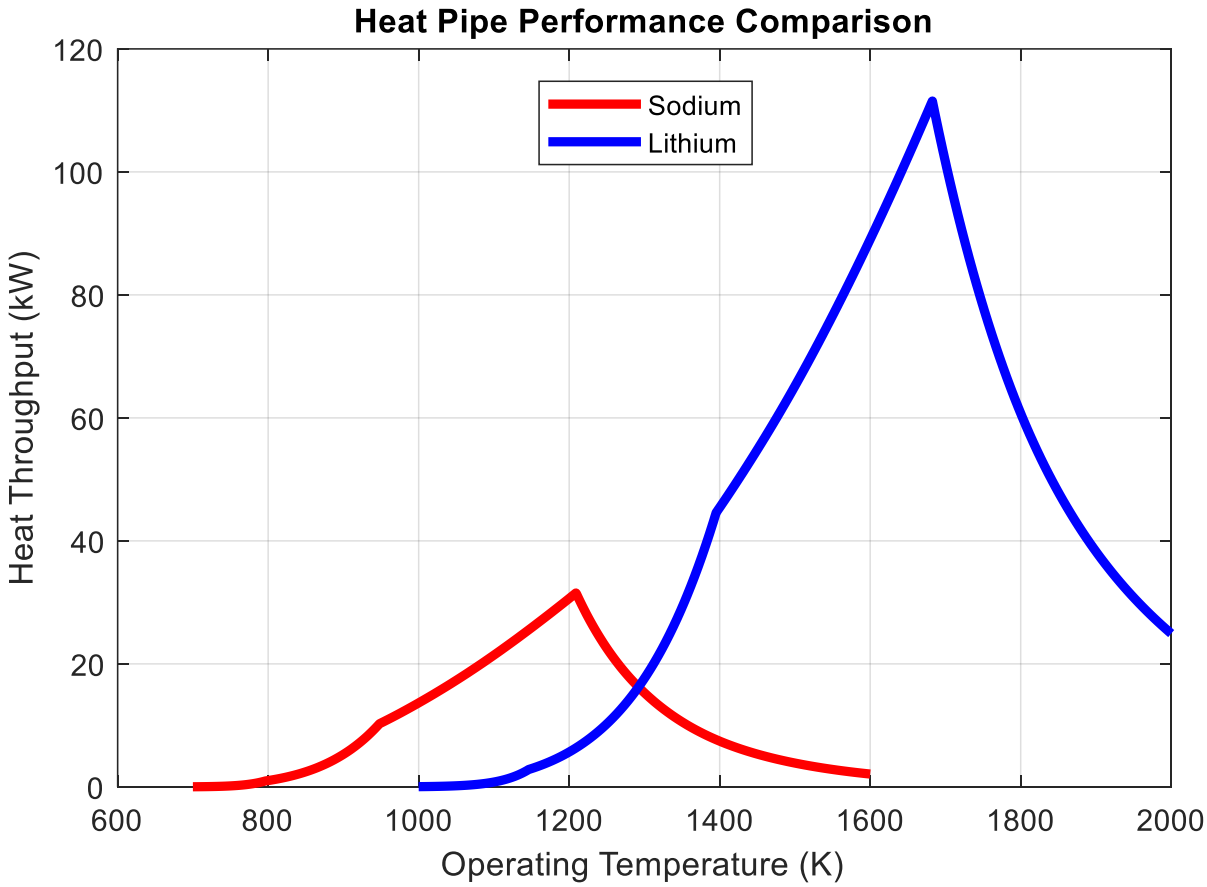

Figure 13: Na and Li Operating Limits

B. Results

Although the heat pipe/reactor/heat exchanger subsystem was allowed to converge anywhere between the desired PCIT and the maximum surface temperature of 1700 K for Li and 1300 K for Na, each heat pipe fluid-PCIT pair case converged to the maximum surface temperature. This suggests that if the reactor is allowed to be much hotter than the PCIT, then the benefit will be mass minimization. Therefore, it is important to consider the reactor temperature limitation as this will be the temperature at which the heat pipes will converge and thus establishing a limit. This convergence is due to the much higher heat transfer available from convection in the heat exchanger when the temperature difference is as high as it can be. When the heat throughput of the heat pipes at the different temperatures as shown in Figure 13 is considered, it is readily seen that the heat throughput potential of Li heat pipes at the converged surface temperature (1700 K) is several times greater than that of the Na heat pipes at their converged surface temperature (1300 K). This results in a much smaller number heat pipes for the Li-based system as shown in Figure 14.

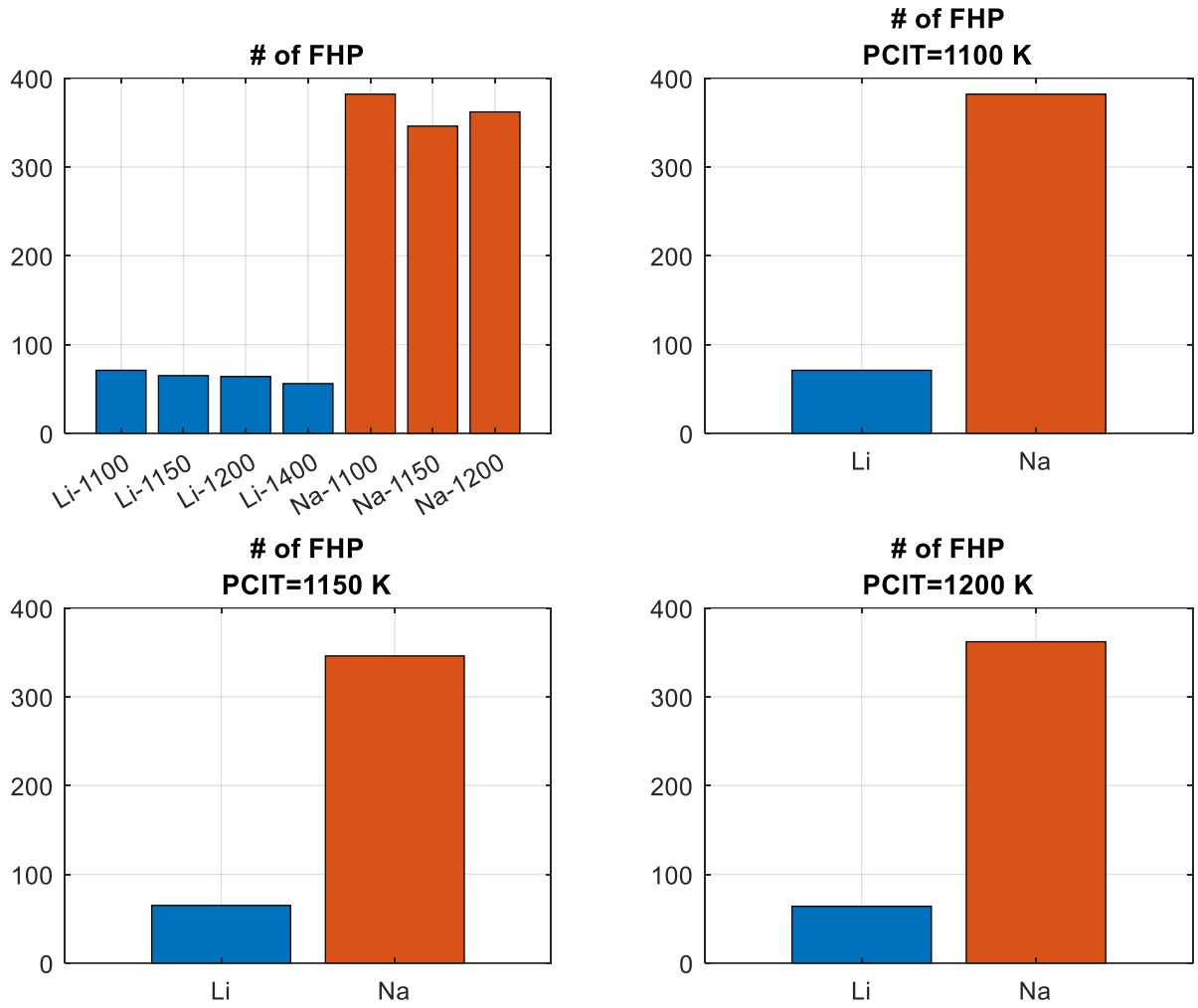

Figure 14: Number of Heat Pipes Comparison

The smaller number of heat pipes in the Li heat pipe subsystem results in a subsystem with a lower mass as shown in Figure 15. Here, the masses of the subsystem components, which include the heat exchanger (heat pipes are in this mass), reactor, and shield, and the total masses of the subsystems are shown for each PCIT-heat pipe fluid pair. The immediate difference between the Li and Na based subsystems is that the Na based subsystem has about three times more mass than the Li based subsystem. Furthermore, it is shown that the Na heat pipe heat exchanger contributes to the mass much more significantly than the Li heat pipe heat exchanger. This is partially due to a larger number of heat pipes, as was shown in Figure 14, yielding to an overall larger heat exchanger.

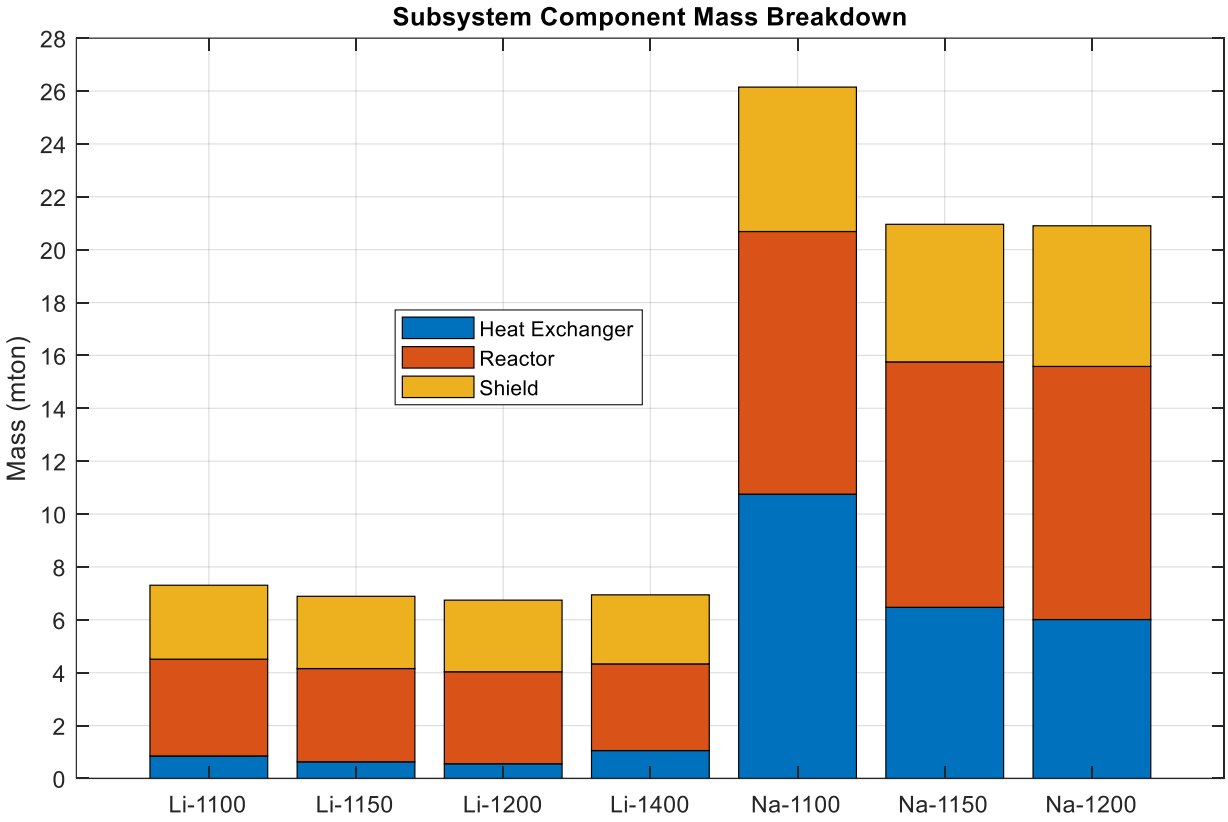

Figure 15: Heat Pipe/Reactor/Heat Exchanger Subsystem Mass Breakdown

Aside from the differences in the masses between the two heat pipe fluids, there are also differences in the mass distributions as shown in Figure 16. Here, the average component percent mass contributions are broken down into the heat exchanger (HX), reactor, and shield and compared between the two considered heat pipe fluids. The key difference in the mass contribution is that the Li heat pipe heat exchanger contributes about a third of the mass than what the Na heat pipe heat exchanger contributes which was also discussed previously and shown in Figure 15. This is attributed to the low heat throughput of the Na heat pipes resulting in a larger array of heat pipes and thus a larger overall heat exchanger fraction.

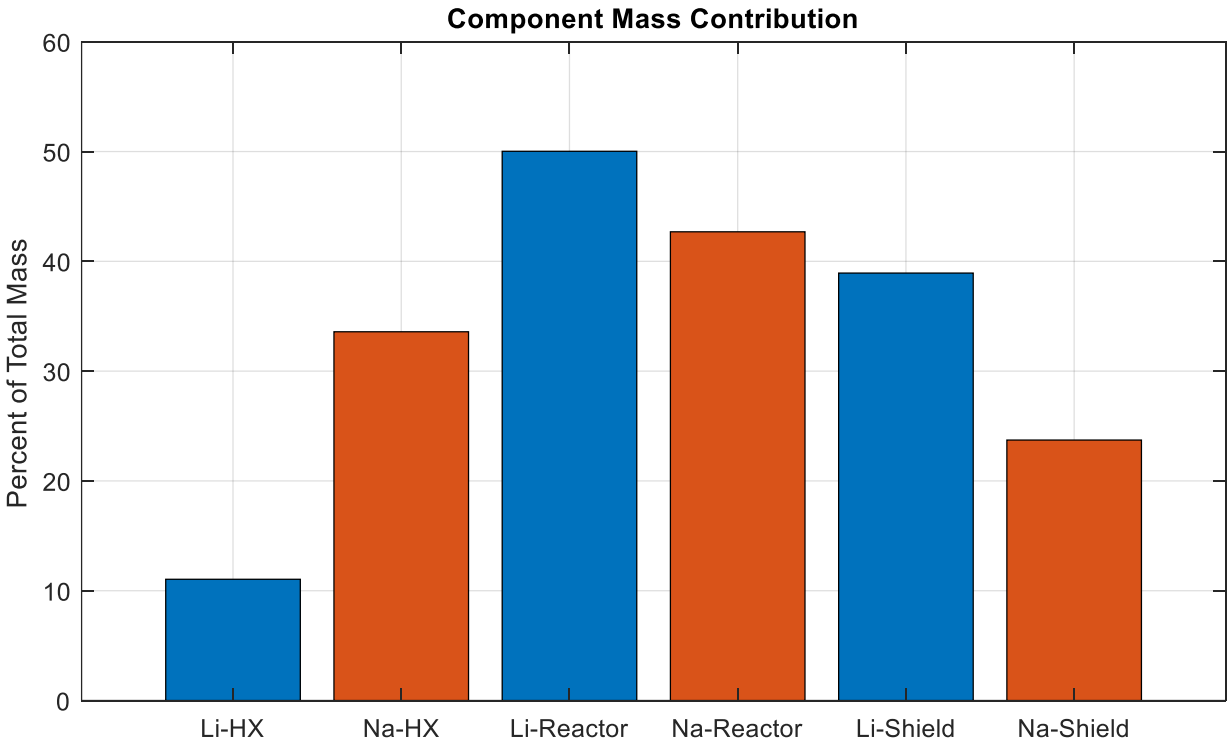

Figure 16: Component Mass Contribution

Figure 17 shows the effects on the pressure losses for the considered heat pipe fluid-PCIT pairs. The pressure losses from Li are affected by the small heat exchanger flow area which results from the low number of heat pipes. Conversely, the Na system has more heat pipes, a larger heat exchanger, and therefore a larger overall flow area in between the heat pipes. However, because of the much larger number of heat pipes in the Na subsystem, frictional pressure losses on the heat pipe surfaces begin to significantly contribute to the overall pressure losses. Moreover, as the PCIT increases, the heat exchanger mass decreases as the cycle becomes more efficient. Based on this, the lowest pressure loss incurred is from the Na 1100 K PCIT subsystem of 2 kPa. The largest pressure loss is from the Li 1400 K PCIT subsystem of around 17 kPa. An interesting concurrence is that both the Li and Na 1150 K PCIT subsystems exhibit very similar pressure losses of around 5 kPa. This is caused by higher Brayton fluid velocity due to the constrained flow area of the Li heat exchanger and the high frictional pressure losses in the Na subsystem balancing each other out and resulting in the observed similar overall pressure losses. For the 1200 K PCIT case, the increasing number of heat pipes in the Na subsystem results in a higher overall pressure loss than in the Li subsystem. In the Li 1400 K PCIT case, the contributions of heating the Brayton fluid to these high temperatures and the low cross sectional flow area result in the highest pressure losses of all considered cases.

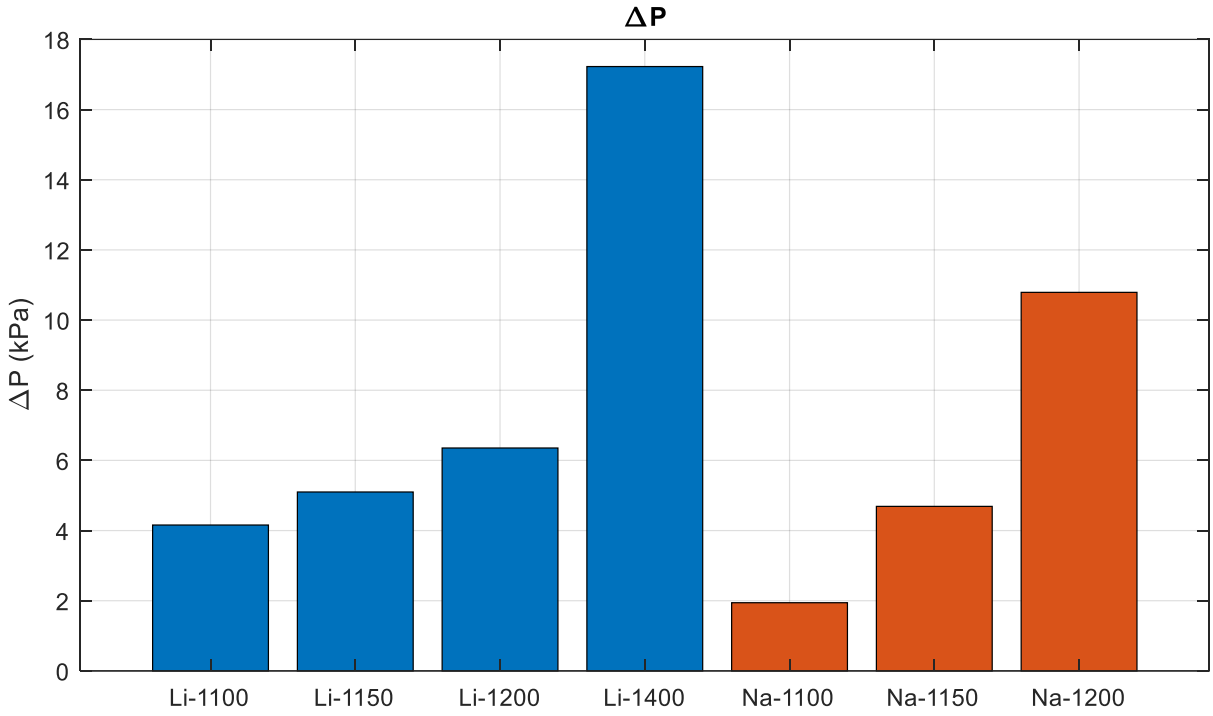

Figure 17: Pressure Losses

VI. CONCLUSION

This paper considered a nuclear electric propulsion (NEP) system power conversion Brayton cycle with a heat pipe reactor. A heat pipe limitations model was used in conjunction with tube bank convective heat transfer and pressure loss correlations from Zukauskas for heat transfer from the reactor to the Brayton fluid. Parametric sizing of the reactor component involved operational limits-based heat pipe thermal hydraulic modeling in cohesion with required user input geometry for the in-core lattice and various subcomponents. The mass of the reactor was based on the scaling of the unit cells according to the total required power to heat the Brayton fluid to a specified power conversion inlet temperature (PCIT). The shield, heat pipe, and heat exchanger masses were based on the first principle approach of volume (geometry) and density.

Na and Li were considered as viable candidates as fluids inside the heat pipes due to their high temperature applications. A limitation of this analysis is that the heat pipe geometry assumption was held constant for both fluids at a value based on a LANL design. Based on this assumption, the maximum heat throughput of Li was around five times greater than that of Na. For the Li-based subsystem, the considered PCITs included 1100 K, 1150 K, 1200 K, and 1400 K in occordance to previous work. Conversely, due to the lower operating temperatures of Na, the Na-based subsystem considered PCITs of 1100 K, 1150 K, and 1200 K with the ommision of the 1400 K PCIT. This resulted in the reactor requiring five times more Na heat pipes than Li heat pipes for the PCITs common for the two fluids. Furthermore, Li's maximum heat throughput peaked at 1700 K while Na's peaked at 1300 K, based on the geometry from LANL, resulting in a larger required heat exchanger for the Na heat pipes which contributed to around a third of the total mass of the subsystem. The higher temperature Li heat pipes, on the other hand, resulted in a heat exchanger mass of about a tenth of the entire subsystem. The pressure losses were also highly affected by the

heat exchanger geometry. The larger heat exchanger of the Na heat pipes at the 1100 K PCIT resulted in the smallest pressure losses as the total cross section flow area offset the losses incurred by friction. However, at the higher PCITs, the Na-based subsystem matched the pressure losses of Li at 1150 K while at 1200 K, the frictional pressure losses contributed significantly to the overall pressure losses for the Na subsystem. At the 1400 K PCIT, the Li-based subsystem exhibited the largest pressure losses due to the low density of the Brayton working fluid at this temperature.

Given the assumptions and the results of the correlations used in this study, Li exhibits superior performance to Na as a heat pipe working fluid for a heat pipe cooled reactor operating at temperatures characteristic for NEP appplications. However, given the uncertainties of these calculations and the constant heat pipe geometry assumption, it cannot be decisevly recommended that Li should be used as the heat pipe fluid of choice for the NEP reactor/heat exchanger subsystem. Future work will need to investigate different geometries and their effects on the reactor unit cell performance. Moreover, an experiment on low Prandtl number fluid flow through tube banks will need to be conducted to conclusively understand the validity of Zukauskas correlations for this thermofluid application and possibly suggest new correlations.

ACKNOWLEDGMENTS

A special thank you to DV Rao for his input and guidance.

This work was supported by NASA's Space Technology Mission Directorate (STMD) through the Space Nuclear Propulsion (SNP) project. This work was funded under Contract No. 80LARC17C0003.

REFERENCES

[1] Chaplin, V. H., Goebel, D. M., Lewis, R. A., Lockwood Estrin, F., and Randall, P. N. "Accelerator Grid Life Modeling of T6 Ion Thruster for BepiColombo." *Journal of Propulsion and Power*, Vol. 37, No. 3, 2021, pp. 436–449. https://doi.org/10.2514/1.B37938.

[2] Robbins, W. H., and Finger, H. B. *An Historical Perspective of the NERVA Nuclear Rocket Engine Technology Program*. Publication NASA-CR-187154. Analytical Engineering Corporation, 1991.

[3] Aerojet Rocketdyne. RL10 Propulsion System. https://www.rocket.com/sites/default/files/documents/Capabilities/PDFs/RL10_data_sheet.pdf.

[4] Duchek, M., Clark, M., Pensado, A., Harnack, C., Machemer, W., and Grella, E. Sensitivity of Hybrid NEP-Chemical Vehicle Mass to Assumptions for Crewed Opposition-Class Mars Missions. Presented at the Propulsion and Energy Forum, Virtual Event, 2021.

[5] Duchek, M., Clark, M., Pensado, A., Harnack, C., Machermer, W., Grella, E., and Qu, M. HYBRID NEP-CHEMICAL VEHICLE AND PROPULSION TECHNOLOGY STUDY FOR CREWED MARS MISSIONS. Presented at the 68th JANNAF Propulsion Meeting, Virtual Event, 2021.

[6] Harnack, C., Machemer, W., Duchek, M., Grella, E., Nikitaev, D., and Smith, C., D. Brayton Cycle Power Conversion Model for MW-Class Nuclear Electric Propulsion Mars Missions. Cleveland, OH, 2022.
[7] Palomares, K., Harnack, C., Smith, C., Herner, R., Machemer, W., Rawlins, S., Grella, E., and Boylston, A. Nuclear Space System Analysis and Modelling (NSSAM): A Software Tool to Efficiently Analyze the Design Space of Space Reactor Systems. Presented at the Nuclear and Emerging Technologies for Space, Virtual Event, 2021.
[8] Li, H., Jiang, X., Chen, L., Ning, Y., Pan, H., and Tengyue, M. "Heat Transfer Capacity Analysis of Heat Pipe for Space Reactor." *At. Energ. Sci. Tech.*, Vol. 49, No. 1, 2015, p. 7. https://www.aest.org.cn/CN/10.7538/yzk.2015.49.01.0089.
[9] Tournier, J.-M. Reactor Lithium Heat Pipes for HP-STMCs Space Reactor Power System. In *SPACE TECHNOLOGY AND APPLICATIONS INTERNAT.FORUM-STAIF 2004: Conf.on Thermophys.in Microgravity; Commercial/Civil Next Gen.Space Transp.; 21st Symp.Space Nuclear Power & Propulsion; Human Space Explor.; Space Colonization; New Frontiers & Future Concepts*, No. 699, Albuquerque, New Mexico (USA), 2004, pp. 781–792.
[10] El-Genk, M. S., and Tournier, J.-M. P. "USES OF LIQUID-METAL AND WATER HEAT PIPES IN SPACE REACTOR POWER SYSTEMS." *Frontiers in Heat Pipes*, Vol. 2, No. 1, 2011. https://doi.org/10.5098/fhp.v2.1.3002.
[11] Moriarty, M. P. *Heat Pipe Cooled Heat Rejection Subsystem Modeling for Nuclear Electric Propulsion*. Publication CR-191132. Rockwell International - Rocketdyne Division, Canoga Park, CA, 1993.
[12] Machemer, W., Duchek, M., and Harnack, C. Mass Sizing Study for NEP Power Conversion Concepts. Presented at the Nuclear Emerging Technologies for Space, Cleveland, OH, 2022.
[13] Nikitaev, D. Nuclear Electric Propulsion Modular Power Conversion Model. Cleveland, OH, 2022.
[14] Ku, J. Introduction to Heat Pipes. NASA/Goddard Space Flight Center, , 2015.
[15] Zuo, Z. J., and Faghri, A. "A Network Thermodynamic Analysis of the Heat Pipe." *International Journal of Heat and Mass Transfer*, Vol. 41, No. 11, 1998, pp. 1473–1484. https://doi.org/10.1016/S0017-9310(97)00220-2.
[16] Guo, Y., Su, Z., Li, Z., and Wang, K. "The Super Thermal Conductivity Model for High-Temperature Heat Pipe Applied to Heat Pipe Cooled Reactor." *Frontiers in Energy Research*, Vol. 10, 2022, p. 819033. https://doi.org/10.3389/fenrg.2022.819033.
[17] Chi, S. W. *Heat Pipe Theory and Practice: A Sourcebook*. Hemisphere Pub. Corp, Washington, 1976.
[18] Busse, C. A. Pressure Drop in the Vapor Phase of Long Heat Pipes. United States, 1967.
[19] Reid, R. S. Heat Pipe Transient Response Approximation. In *SPACE TECHNOLOGY AND APPLICATIONS INTERNATIONAL FORUM- STAIF 2002*, No. 608, Albuquerque, New Mexico (USA), 2002, pp. 156–162.
[20] Brown, O. L. I. "The Clausius-Clapeyron Equation." *Journal of Chemical Education*, Vol. 28, No. 8, 1951, p. 428. https://doi.org/10.1021/ed028p428.
[21] Reay, D. A., Kew, P. A., and McGlen, R. J. *Heat Pipes: Theory, Design and Applications*. Butterworth-Heinemann, an imprint of Elsevier, Amsterdam, 2014.
[22] Churchill, S. W. "Friction-Factor Equation Spans All Fluid-Flow Regimes." *Journal of Chemical Engineering*, Vol. 84, No. 24, 1977, pp. 91–92.

[23] Zohuri, B. *Heat Pipe Design and Technology: Modern Applications for Practical Thermal Management*. Springer International Publishing : Imprint: Springer, Cham, 2016.
[24] Levy, E. K. "Theoretical Investigation of Heat Pipes Operating at Low Vapor Pressures." *Journal of Engineering for Industry*, Vol. 90, No. 4, 1968, pp. 547–552. https://doi.org/10.1115/1.3604687.
[25] Deverall, J. E., Kemme, J. E., and Florschuetz, L. W. *Sonic Limitations and Startup Problems of Heat Pipes*. Publication LA4518. Los Alamos Scientific Laboratory, Los Alamos, NM, 1970.
[26] Tien, C. L., and Chung, K. S. "Entrainment Limits in Heat Pipes." *AIAA Journal*, Vol. 17, No. 6, 1979, pp. 643–646. https://doi.org/10.2514/3.61190.
[27] Mayorca, M. A. *Numerical Methods for Turbomachinery Aeromechanical Predictions*. Dissertation. Royal Institute of Technology, Stockholm, Sweden, 2011.
[28] Beard, D., Tarau, C., and Anderson, W. G. Sodium Heat Pipes for Space and Surface Fission Power. Presented at the 15th International Energy Conversion Engineering Conference, Atlanta, GA, 2017.
[29] King, D. B., and Marshall, A. C. RSMASS-D Nuclear Thermal Propulsion and Bimodal System Mass Models. Presented at the AIP Conference Proceedings Volume 387, Albuquerque, New Mexico (USA), 1997.
[30] J Ashcroft and C Eshelman. *Summary of NR Program Prometheus Efforts*. Publication LM-05K188, 881290. 2006, p. LM-05K188, 881290.
[31] StructX. Plate Fixed On All Edges with Uniform Load. StructX, , 2022.
[32] D'Errico, J. 1.4.0.0. *Fminsearchbnd, Fminsearchcon*. MathWorks, 2012.
[33] Žukauskas, A. Heat Transfer from Tubes in Crossflow. In *Advances in Heat Transfer*, Elsevier, 1972, pp. 93–160.
[34] El-Genk, M., and Gallo, B. High Performance Brayton Rotating Unit (UNM-BRU-3) for Space Reactor Power Systems. Presented at the 7th International Energy Conversion Engineering Conference, Denver, Colorado, 2009.
[35] Huber, M. L. *Models for Viscosity, Thermal Conductivity, and Surface Tension of Selected Pure Fluids as Implemented in REFPROP V10.0*. Publication NIST IR 8209. National Institute of Standards and Technology, Gaithersburg, MD, 2018, p. NIST IR 8209.
[36] Bell, I. H., Wronski, J., Quoilin, S., and Lemort, V. "Pure and Pseudo-Pure Fluid Thermophysical Property Evaluation and the Open-Source Thermophysical Property Library CoolProp." *Industrial & Engineering Chemistry Research*, Vol. 53, No. 6, 2014, pp. 2498–2508. https://doi.org/10.1021/ie4033999.
[37] Çengel, Y. A., and Ghajar, A. J. *Heat and Mass Transfer: Fundamentals & Applications*. McGraw Hill Education, New York, NY, 2015.
[38] Incropera, F. P., and DeWitt, D. P. *Fundamentals of Heat and Mass Transfer*. J. Wiley, New York, 2002.
[39] Mills, A. F., and Coimbra, C. F. M. *Heat Transfer*. 2016.
[40] Daney, David E. *Effect of Noble Gas Mixtures on the Performance of Regenerative-Type Cryocoolers Analytical Estimate*. Publication NISTIR 90-3936. National Institute of Standards and Technology, Boulder, CO, 1990.
[41] Daney, D. E. "Regenerator Performance with Noble Gas Mixtures." *Cryogenics*, Vol. 31, No. 10, 1991, pp. 854–861. https://doi.org/10.1016/0011-2275(91)90017-Q.
[42] Jiro. 1.0.0.1. *GRABIT*. MATLAB Central File Exchange, 2016.

[43] Bartz, D. R. “A Simple Equation for Rapid Estimation of Rocket Nozzle Convective Heat Transfer Coefficients.” *Journal of Jet Propulsion*, Vol. 27, No. 1, 1957, pp. 49–53. https://doi.org/10.2514/8.12572.
[44] Tizón, J. M., and Roman, A. A Mass Model for Liquid Propellant Rocket Engines. Presented at the 53rd AIAA/SAE/ASEE Joint Propulsion Conference, Atlanta, GA, 2017.
[45] McGuire, M. L. Use of High-Power Brayton Nuclear Electric Propulsion (NEP) for a 2033 Mars Round-Trip Mission. In *SPACE TECH.& APPLIC.INT.FORUM-STAIF 2006: 10th Conf Thermophys Applic Microgravity; 23rd Symp Space Nucl Pwr & Propulsion; 4th Conf Human/Robotic Tech & Nat’l Vision for Space Explor.; 4th Symp Space Coloniz.; 3rd Symp on New Frontiers & Future Concepts*, No. 813, Albuquerque, New Mexico (USA), 2006, pp. 222–229.
[46] Zukauskas, A. and Ulinskas, R. *Heat Transfer in Tube Banks in Crossflow*. United States, 1988.
[47] Mason, L. S. Power Technology Options for Nuclear Electric Propulsion. Presented at the 2002 37th Intersociety Energy Conversion Engineering Conference (IECEC), Washington, WA, USA, 2004.